Journal of
Materials Chemistry B

Materials for biology and medicine

Accepted Manuscript

This article can be cited before page numbers have been issued, to do this please use: M. Liu, J. Li, Z. Wang, M. Chen, J. Yi, Z. Zhao and K. Liang, *J. Mater. Chem. B*, 2025, DOI: 10.1039/D5TB01477H.

This is an Accepted Manuscript, which has been through the Royal Society of Chemistry peer review process and has been accepted for publication.

Accepted Manuscripts are published online shortly after acceptance, before technical editing, formatting and proof reading. Using this free service, authors can make their results available to the community, in citable form, before we publish the edited article. We will replace this Accepted Manuscript with the edited and formatted Advance Article as soon as it is available.

You can find more information about Accepted Manuscripts in the Information for Authors.

Please note that technical editing may introduce minor changes to the text and/or graphics, which may alter content. The journal's standard Terms & Conditions and the Ethical guidelines still apply. In no event shall the Royal Society of Chemistry be held responsible for any errors or omissions in this Accepted Manuscript or any consequences arising from the use of any information it contains.

ROYAL SOCIETY OF CHEMISTRY

rsc.li/materials-b

View Article Online
DOI: 10.1039/D5TB01477H

Multifunctional PAMAM Nanoparticles with Sequential Antimicrobial-Remineralization Therapy for Dentin Caries Management

Mingxiao Liu [a,b], *Jiahe Li* [a,c], *Ziyou Wang* [a,c], *Miao Chen* [a,b], *Jianru Yi* *[a,b], Zhihe Zhao *[a,b], *Kunneng Liang* *[a,c]

M. Liu, J. Li, Z. Wang, M. Chen, J. Yi, Z. Zhao, K. Liang

State Key Laboratory of Oral Diseases, National Center for Stomatology, National Clinical Research Center for Oral Diseases, Sichuan University, Chengdu 610041, China

M. Liu, M. Chen, J. Yi, Z. Zhao

Department of Orthodontics, West China Hospital of Stomatology, Sichuan University, Chengdu 610041, China

J. Li, Z. Wang, K. Liang

Department of Cariology and Endodontics, West China Hospital of Stomatology, Sichuan University, Chengdu 610041, China

* Corresponding authors.

E-mail: kunnengliang@scu.edu.cn (Prof. K. Liang), zhzhao@scu.edu.cn (Prof. Z. Zhao), jianruyi@scu.edu.cn (Prof. J. Yi)

Keywords:

dentin caries, antimicrobials, matrix metalloproteinases, collagen, PAMAM dendrimers, remineralization

View Article Online
DOI: 10.1039/D5TB01477H

Abstract

Dentin caries represents a multifactorial pathological process characterized by bacterial colonization and biofilm formation that result in concurrent acid-mediated demineralization and matrix metalloproteinases (MMPs)-mediated degradation of the collagenous matrix. While remineralization therapies offer minimal invasiveness, their long-term efficacy is compromised by ongoing collagen degradation and persistent bacterial acid production that counteract remineralization efforts. To address these limitations, we designed PAMAM-G4@EG (PGE) nanoparticles (NPs) using polyamide amine (PAMAM) dendrimers as mineral deposition templates, with antimicrobial peptide $G(IIKK)_4I\text{-}NH_2$ (G4) grafted onto the external surface groups and epigallocatechin gallate (EG) encapsulated within the internal cavities to provide biofilm disintegration and collagen protection for comprehensive dentin caries intervention. First, the PGE NPs reach lesion surfaces and accelerate EG release under acidic conditions. EG loosens *Streptococcus mutans* (*S. mutans*) biofilms, followed by G4-mediated disruption of planktonic *S. mutans* cell membranes. *In vitro* antimicrobial assays demonstrated a bactericidal efficacy of 99.75% after PGE intervention. Upon deeper lesion penetration, PGE releases EG to inhibit MMPs activity and preserve the collagen scaffold, achieving a 74% reduction in hydroxyproline (HYP) levels. Simultaneously, PAMAM promotes controlled hydroxyapatite (HA) deposition, facilitating dentin remineralization. Treatment with PGE in artificial saliva containing collagenase restored dentin hardness to 89.88% of intact values. *In vivo* validation using a rat caries model confirmed therapeutic efficacy through significant reductions in Keyes scores, decreased salivary *S. mutans* counts, and increased molar mineral density. These findings demonstrate the therapeutic efficacy of PGE in dentin caries prevention and treatment, supporting its potential for clinical application.

View Article Online
DOI: 10.1039/D5TB01477H

Introduction

Dental caries is one of the most widespread chronic diseases worldwide, affecting over 2.3 billion individuals and imposing substantial socioeconomic burdens through pain, infection, and diminished quality of life. [1] The pathogenesis of caries stems from an imbalance between demineralization and remineralization processes. [2-4] The reason for demineralization is caused by cariogenic bacteria, predominantly *Streptococcus mutans* (*S. mutans*), which metabolize dietary carbohydrates into lactic acid, leading to sustained acid production that dissolves hydroxyapatite (HA) crystals. [5, 6] In dentin caries, unique therapeutic challenges arise from the distinctive composition of dentin, which comprises 20% organic matrix, primarily type I collagen. Matrix metalloproteinases (MMPs) in saliva then degrade the collagenous matrix, dismantling the scaffold essential for dentin mineral deposition. [7, 8] Conventional caries treatment relies on invasive mechanical removal with high-speed rotary instruments, followed by artificial restoration. This method sacrifices healthy tooth structure irretrievably and undermines long-term dental integrity. Remineralization therapies mark a shift toward preserving natural tooth structure by restoring mineral content and mechanical properties through minimally invasive approaches. However, current strategies, such as fluoride therapies and calcium phosphate-based materials, have notable limitations. They fail to address ongoing collagen degradation and persistent bacterial acid production, both of which hinder remineralization and prevent lasting therapeutic success, necessitating advanced multifunctional solutions.

Among various remineralization approaches, polyamide amine (PAMAM) dendrimer stands out due to its exceptional modifiability, enabling the integration of multifunctional capabilities alongside mineral restoration. The dendritic structure of carboxyl-terminated PAMAM (PAMAM-COOH) polymers features abundant carboxyl groups that attract Ca^{2+} and PO_4^{3-} *via* electrostatic interactions, acting as nucleation templates for HA crystal formation. [6, 9] However, clinical application of PAMAM dendrimers also faces the previously mentioned obstacles. First, persistent bacterial activity produces demineralizing acids that diminish therapeutic efficacy. The bacterial extracellular polysaccharide (EPS) matrix further complicates this by forming protective barriers that shield pathogens from salivary clearance, antimicrobial agents,

and host immune responses. [10-12] Second, endogenous MMPs degrade the dentin collagen scaffold, weakening the structural foundation required for mineral deposition. The inherent modifiability of PAMAM dendrimers presents an opportunity to address these limitations, as their external groups allow for molecular grafting while their internal cavities enable drug loading. Therefore, we designed a comprehensive approach utilizing both external surface modification and internal encapsulation to create an advanced PAMAM-based remineralization system for dentin caries intervention.

Epigallocatechin gallate (EG), a bioactive polyphenol derived from green tea, serves as a dual-function therapeutic agent to address enzymatic collagen degradation and bacterial biofilm pathogenicity. EG inhibits MMPs through zinc chelation and disintegrates biofilm architecture by binding to glucosyltransferase residues and suppressing biofilm-formation genes. [13-16] However, its antimicrobial efficacy against planktonic bacteria post-biofilm disintegration remains limited. Thus, we incorporated the synthetic antimicrobial peptide (AMP) $G(IIKK)_4I\text{-}NH_2$ (G4), which adopts an amphiphilic α-helical conformation to insert into and disrupt bacterial membranes, exhibiting superior bactericidal activity against *S. mutans*. [17-20] Our strategy integrates these agents *via* dual modification of PAMAM dendrimers: EG is encapsulated within the dendrimer core for controlled release, while AMP G4 are conjugated to the external surface. Specifically, fourth-generation PAMAM-COOH dendrimers with 64 terminal groups were modified, with 32 AMP G4 attached *via* amide bonds and 32 carboxyl groups reserved for Ca^{2+} and PO_4^{3-} sequestration (Scheme 1a).

The integration of EG encapsulation and G4 conjugation within the PAMAM-COOH scaffold creates PAMAM-G4@EG (PGE) nanoparticles (NPs). In the acidic cariogenic environment, pH-accelerated EG release penetrates and disrupts the protective EPS of plaque biofilms, enabling deeper PGE penetration into demineralized dentin lesions. Following biofilm disintegration, surface-conjugated AMP G4 delivers potent bactericidal effects against liberated planktonic bacteria through membrane disruption and pore formation, halting acid production and fostering a sterile environment for remineralization. Simultaneously, EG sustains MMPs inhibition, preserving the collagen scaffold's integrity. The preserved carboxyl groups on the PAMAM backbone then attract Ca^{2+} and PO_4^{3-}, facilitating deposition of HA.

This engineered approach achieves comprehensive caries management by programmatically integrating bacterial infection, enzymatic degradation, and mineral loss (Scheme 1b).

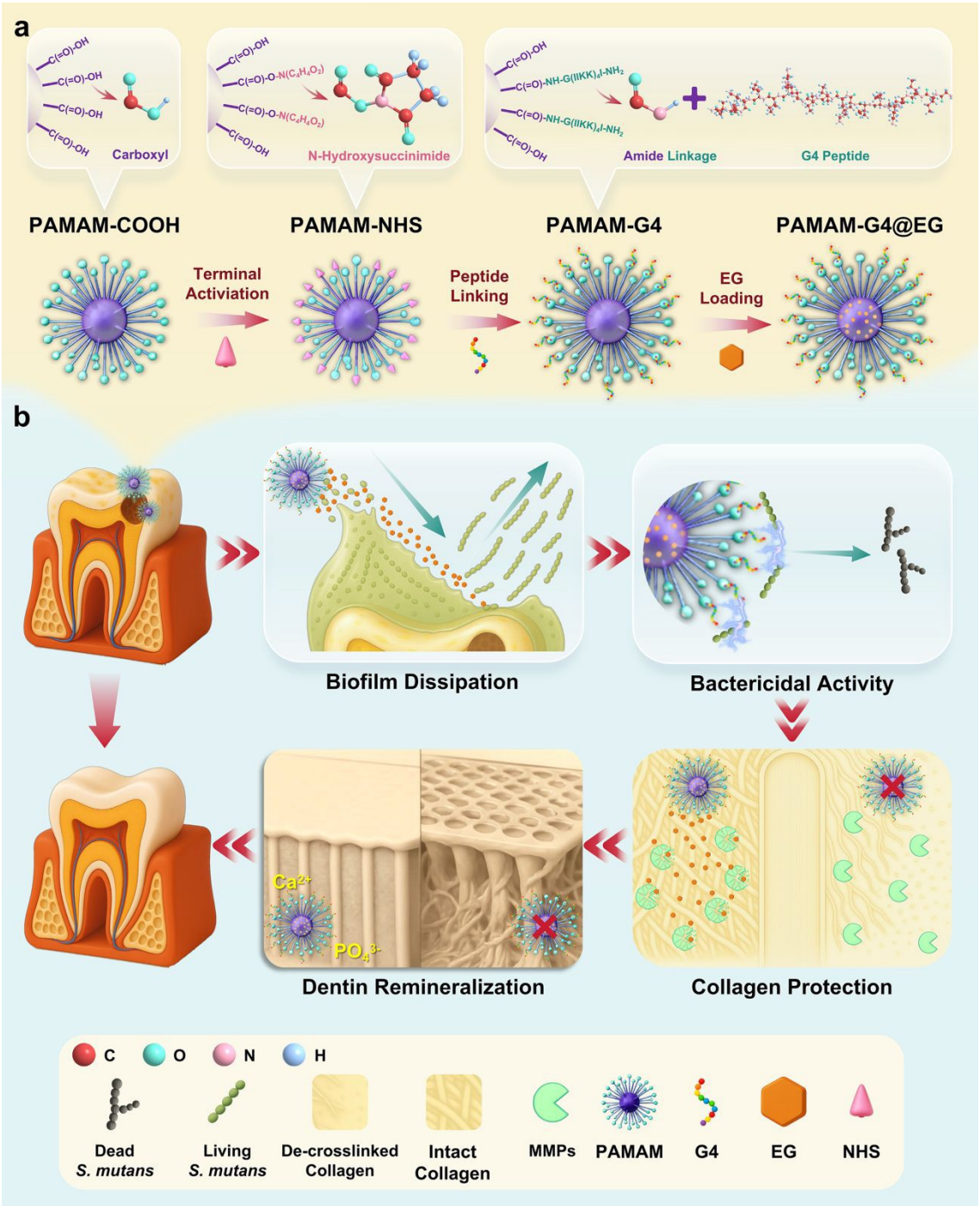

Scheme 1. Nanoplatform for Dentin Regeneration. a) Stepwise synthesis of PGE NPs through sequential functionalization of PAMAM dendrimer cores with AMP G4 conjugation and EG encapsulation. **b)** The therapeutic mechanism of PGE NPs within the dentin-pulp complex shows biofilm disintegrative and bactericidal activity, collagen matrix protection *via* MMPs inhibition, and dentin regeneration through PAMAM-COOH.

View Article Online
DOI: 10.1039/D5TB01477H

Experimental Section

Synthesis, Characterization, and Screening of AMP G4:

The AMP G4 was identified as a promising candidate for investigation through literature reviews. [18] G4 was synthesized using an automatic peptide synthesizer (PSSM-8, Shimadzu, Japan) at Shanghai Bootech BioScience and Technology Company. Peptide purity was analyzed using high-performance liquid chromatography (HPLC, Agilent Technologies, USA) with a 1.0 mL/min flow rate and 220 nm detection wavelength. Mass spectrometry (MS, LCQ Deca XP MAX, USA) performed at 5.02 kV spray voltage and 0.14 mA spray current confirmed the peptide's molecular weight.

Synthesis and Characterization of PAMAM-G4:

Fourth-generation PAMAM-COOH dendrimers were procured from Chenyuan Dendrimer Tech (Weihai, China). Detailed synthesis procedures are documented in the Supporting Information. PAMAM-G4 (PG) purity assessment was conducted *via* HPLC (Agilent Technologies, USA) operating at a 1.0 mL/min flow rate with detection at 220 nm wavelength.

Preparation of EG-loaded Dendrimer:

PAMAM dendrimers (3 mg/mL in double distilled water) were mixed with EG (2 mg/mL in dimethyl sulfoxide) at a 7:1 volume ratio, achieving 9% loading efficiency. The solution underwent continuous agitation for 72 h at 37 °C, followed by centrifugation at 10,000 rpm for 10 min. Clear supernatant containing PGE complexes was collected and subsequently lyophilized. Loading efficiency calculations and experimental protocols are fully documented in the Supporting Information.

Characterizations of PGE and its Components:

PGE preparation and characterization involved comprehensive analytical techniques, with detailed EG release kinetics methodology described in the Supporting Information section.

High-resolution morphological and structural characterization was conducted using field-emission scanning electron microscopy (FE-SEM, Sigma 500, Zeiss, Germany). Elemental distribution mapping was performed through energy-dispersive X-ray spectroscopy (EDS). Particle size distribution and zeta potential were measured using dynamic light scattering (DLS) with a Zetasizer Nano instrument (Malvern, UK). Crystal structure analysis of EG, PG, and PGE was determined *via* X-ray diffraction (XRD, IV, Rigaku, Japan). Thermal properties and phase transitions were evaluated using differential

scanning calorimetry (DSC, METTLER TOLEDO, Switzerland). Molecular characterization included attenuated total reflectance Fourier transform infrared spectroscopy (ATR-FTIR, Nicolet iS10, Thermo Scientific, USA) to identify functional groups and interactions, while detailed molecular structure analysis was performed using proton nuclear magnetic resonance spectroscopy (^{1}H NMR, Bruker Avance spectrometer, AVII-400, Karlsruhe, Germany).

Cytotoxicity Assay:

Human oral keratinocytes (HOKs) and human dental pulp cells (HDPCs) were utilized to evaluate both the concentration-dependent cytotoxicity of PGE and the comparative cytotoxicity of EG, PG, and PGE at predetermined concentrations. Complete methodology for the cytotoxicity assays is provided in the Supporting Information section.

Collagen Stabilization:

Type I collagen degradation was assessed using a hydroxyproline (HYP) quantification approach (detailed in the Supporting Information section).

Antibacterial Capacity *in Vitro:*

Antibacterial efficacy of PGE against *S. mutans* (ATCC 700610) was assessed *in vitro* through standardized broth microdilution assays. Minimum inhibitory concentration (MIC) values were established by spectrophotometric quantifying bacterial growth at 600 nm. Based on MIC results, an effective working concentration was established for subsequent experiments. Antibacterial efficacy was evaluated by treating *S. mutans* cultures with PGE, EG, and PG at this concentration, with viable bacteria quantified by Colony Forming Units (CFUs) calculation using the spread plate method. Mature biofilm disintegration capacity was assessed using SYTO 9/PI double staining to determine live/dead bacterial ratios. Scanning electron microscopy (SEM) and transmission electron microscopy (TEM) visualized bacterial ultrastructure and membrane integrity following treatment.[21]

Anti-biofilm formation properties of PGE against *S. mutans* were assessed employing a human dentin slice model. Biofilms were cultivated under standardized conditions and subsequently analyzed using SYTO 9 fluorescent staining and crystal violet (CV) staining to assess biofilm biomass quantitatively. SEM was employed to evaluate plaque biofilm thickness and bacterial distribution density on dentin slices following PGE treatment.

View Article Online
DOI: 10.1039/D5TB01477H

Remineralization of Demineralized Dentin *in Vitro*:

Dentin specimens underwent preparation processes detailed in the Supporting Information. Specimens underwent demineralization in EDTA solution (0.5 M, pH 8.0) for 30 min at ambient temperature, then incubated with guanidine hydrochloride (4 M, 60 min) to remove non-collagenous proteins. [22] After triple rinses with double distilled water (DDW) and 10 min ultrasonication, specimens were stored in calcium-free phosphate-buffered saline at 4 °C. The study implemented two parallel remineralization models: artificial saliva (AS) with and without collagenase. Demineralized specimens were randomly allocated to treatment groups (n=8 per group per model) and subjected to cyclic treatment every four days. Each specimen received 50 μL of DDW (control), EG, PG, or PGE for 1 h, followed by triple DDW rinses and air-drying. For remineralization, specimens were immersed in 6 mL of either standard AS or collagenase supplemented AS (1.5 U/mL Clostridium histolyticum Type VII collagenase). [22] Solutions were refreshed daily throughout the 20-day experiment. Spent collagenase containing AS was collected daily for HYP quantification to assess collagen degradation.

SEM. Each dentin block was bisected perpendicular to its exposed surface using a low-speed, water-cooled diamond saw (Minitom, Struers, Copenhagen, Denmark). Original exposed and cross-sectional surfaces were sputter-coated with gold to enhance conductivity, then examined *via* SEM (Inspect F50, FEI, USA) to visualize mineral structure morphology.

XRD. XRD analysis (Ultima IV, Rigaku, Japan) was conducted on dentin specimens from three experimental groups across two distinct models, pre- and post-20-day remineralization. Under equivalent analytical conditions, an untreated, intact dentin disk served as a control.

ATR-FTIR. Following the 20-day remineralization period, dentin specimens were rinsed with DDW, air-dried, and analyzed *via* ATR-FTIR spectroscopy (NICOLET iS10, Thermo Scientific, USA).

Vickers Hardness Measurement. Microhardness evaluation of specimens from three experimental groups across two models was performed at 5, 10, 15, and 20-day intervals. Vickers hardness testing employed a diamond indenter (25 gf load, 10 s duration) using an MMT-X7A system (Matsuzawa, Japan), with five indentations per specimen. Healthy and etched, untreated dentin served as controls.

White Light Interferometer. To characterize surface morphology, dentin blocks were analyzed with white-light interferometry (Up-3000, Rtec Instruments Inc., USA).

View Article Online
DOI: 10.1039/D5TB01477H

Comprehensive Caries Management *in Vivo*:

Ethical Approval. The animal experiments were conducted following approval from the Ethics Committee of the Hospital of Stomatology, Sichuan University, China (Approval No. WCHSIRB-D-2018-030).

Animal Model and Housing. Specific pathogen-free male Sprague Dawley (SD) rats were obtained from Da-Shuo Animal Center (Sichuan, China), weaned at 17 days of age, and acclimated for three days under controlled conditions (22 ± 2 °C, 55 ± 5% humidity, 12 h light/dark cycle). Initial body weights were recorded to ensure group uniformity. Animals were housed in individually ventilated cages to minimize cross-contamination, with access to sterile bedding and environmental enrichment. Complete dietary protocols are detailed in the Supporting Information.

Bacterial Infection. Following acclimation, SD rats were orally infected with *S. mutans* (ATCC 700610) to establish a caries-prone oral microbiome. The infection protocol is detailed in the Supporting Information. Infection was confirmed by microbial sampling of oral swabs using the smear plate method to verify colonization consistency before initiating treatment.

Caries Treatment. Following confirmed bacterial infection, SD rats were randomly distributed into four groups (n=5 per group) using a randomized block design to eliminate bias. The control group received DDW, while the experimental groups were treated with NPs formulations. Treatments were applied topically to molars using sterile cotton swabs, with each rat receiving 400 μL of solution (100 μL per quadrant for 15 s). Applications occurred twice daily (8:00 a.m. and 8:00 p.m.) for 4 weeks, simulating regular oral hygiene practices. To prevent dilution and enhance contact time with active compounds, water access was restricted for 1 h after each treatment.

Sample Collection. Weekly saliva collection using cotton swabs and body weight monitoring were conducted throughout the four-week treatment period. Following study completion, animals were euthanized and mandibles, maxillae, oral mucosa, and major organs (heart, liver, spleen, lung, kidney) were harvested. Tissue specimens underwent fixation in 10% neutral buffered formalin for 48 h to preserve structural integrity.

Histological Analysis. To compare treatment effects, buccal and lingual mucosa samples from control and PGE groups were selected for histological evaluation. Tissues underwent dehydration, paraffin embedding, and were sectioned at 5 μm thickness. Hematoxylin and eosin (H&E) staining visualized

cellular and extracellular matrix structures. Light microscopy assessment evaluated inflammation, epithelial integrity, and mucosal changes. For systemic biocompatibility evaluation, histological sections of heart, liver, spleen, lung, and kidney tissues from euthanized rats were similarly processed and examined for pathological alterations.

Caries Scoring (Keyes Method). Left halves of maxillae and mandibles were rinsed with DDW, stained with 0.4 mg/mL murexide for 12 h, and hemisectioned along the mesiodistal sagittal plane. According to the Keyes scoring method, pit and fissure caries were assessed *via* stereoscopic microscopy. [23] A single examiner performed all evaluations, with verification by two independent reviewers to ensure inter-examiner reliability.

Micro-CT Scanning and Analysis. Right mandibular halves underwent micro-CT scanning (μCT50, SCANCO, Switzerland) at 70 kV, 200 μA, with 10 μm isotropic voxel resolution. Three-dimensional reconstruction was performed *via* SCANCO Visualizer 1.1.18.0, while dentin mineral density within 200 μm beneath the enamel was quantified through SCANCO Evaluation 1.1.19.0.

Statistical Analysis:

Statistical analysis was conducted *via* SPSS software version 21.0 (IBM, Chicago, IL, USA). Data normality was assessed through the Kolmogorov-Smirnov test. Unpaired Student's t-tests facilitated two-group comparisons with significance established at $p = 0.05$, while one-way analysis of variance detected differences among three or more groups.

Results and Discussion

Preparation and Characterization of PGE:

Characterization of AMP G4. AMP G4 was synthesized using established solid-phase peptide synthesis protocols. The molecular structure was validated through computational modeling with Chem3D (v18.0, USA). Structural diagrams are shown in Figure S1a. HPLC analysis demonstrated purity exceeding 95%, confirming successful isolation of the target AMP (Figure S1b). MS analysis yielded a molecular weight of 2118.90 g/mol. This closely aligned with the theoretical molecular weight of 2116.87 g/mol calculated from the amino acid sequence (Figure S1c). These analytical data collectively confirm the successful synthesis and

View Article Online
DOI: 10.1039/D5TB01477H

purification of AMP G4.

Confirmation of PGE NPs Synthesis. EDS elemental mapping revealed uniform distribution of carbon (C), oxygen (O), and nitrogen (N) elements throughout the NPs' structure, confirming homogeneous component integration (Figure 1a). Quantitative elemental analysis revealed a C/N ratio of 3.1 and a C/O ratio of 2.65, significantly lower than theoretical ratios for pristine fourth-generation PAMAM dendrimers. The elevated nitrogen content confirms successful AMP G4 conjugation to the dendrimer scaffold, while increased O content validates effective EG encapsulation within the nanocarrier system. FE-SEM analysis revealed that the synthesized PGE formulation self-assembled into well-defined spherical NPs with remarkable uniformity and minimal aggregation (Figure 1b). Complementary DLS measurements confirmed a mean hydrodynamic diameter of 164.2 nm with a narrow size distribution (Figure 1c). The polydispersity index was less than 0.2, indicating excellent colloidal stability and batch homogeneity. The NPs exhibited a negative surface charge with a zeta potential of -19.5 mV (Figure 1d), within the optimal range (-15 to -30 mV) for electrostatic repulsion between NPs.

Verification of EG Loading. XRD analysis revealed distinct crystalline peaks in the EG spectrum, indicating an ordered molecular arrangement (Figure 1e). The PG spectrum exhibited a characteristic broad peak typical of amorphous materials. PGE demonstrated a similar non-crystalline pattern, suggesting successful molecular dispersion of EG within the dendrimer matrix. DSC showed the absence of thermal transitions in PG samples (Figure 1f). EG displayed an endothermic peak at 154.1 °C that was absent in the PGE thermogram. This indicates complete drug encapsulation and molecular interactions inhibiting crystallization. The *in vitro* release profiles of EG demonstrated pH-accelerated kinetics (Figure 1g). Enhanced liberation occurred under cariogenic conditions (pH 5.5) compared to physiological (pH 7.0) conditions. At 24 h, release was 62.61% versus 55.44%, respectively. At 144 h, cumulative release reached 90.59% versus 86.30%. This pH-accelerated behavior enables PGE to deliver EG rapidly in caries-prone conditions. The incomplete release results from steric hindrance within PAMAM's nanoscale cavities and electrostatic interactions between anionic PAMAM-COOH and EG's hydroxyl groups. ATR-FTIR spectroscopy provided molecular fingerprinting

of the nanocarrier systems (Figure 1h). The EG spectrum displayed characteristic aromatic peaks at 1614–1446 cm^{-1} (benzene ring skeletal vibrations). These peaks persisted in the PGE spectrum, confirming retention of EG's chemical structure. Analysis of the peptide-dendrimer framework revealed preserved amide vibrations in both PG and PGE spectra. These included amide I band (C=O stretching, ~1641 cm^{-1}), amide II band (N-H bending, ~1544 cm^{-1}), and amide III band (C-N stretching, ~1395 cm^{-1}). This indicates retained molecular integrity during encapsulation. ^{1}HNMR analysis confirms the composition of the PGE composite, comprising PG and EG (Figure 1i). The dimethyl sulfoxide (DMSO) solvent peak at ~2.50 ppm served as a reference. The spectrum exhibits characteristic signals from both components. PG-specific resonances include amide protons (R-CONH-R, ~7.5–8.5 ppm, peak g) and methylene protons adjacent to tertiary amines ($N(CH_2CH_2CO–R)3$, ~2.0–3.0 ppm, peak a). EG-specific signals include aromatic protons (R-Ph-H, ~6.0–8.0 ppm, peaks d, e, f), methine protons (R-CHOR-CHR_1R_2, ~4.0–5.5 ppm, peak c), and aliphatic protons (CHR_1R_2-CHOR-R, ~2.5–4.0 ppm, peak b). The PGE spectrum contains all these characteristic peaks, indicating successful loading of EG.

From Generation 4 onward, PAMAM dendrimers adopt a spheroidal conformation that enhances therapeutic agent encapsulation. [24, 25] In drug delivery applications, PAMAM dendrimers serve as carriers for poorly soluble molecules. They utilize non-covalent interactions, including hydrogen bonding, electrostatic forces, and hydrophobic effects. [26] This improves solubility and protects against degradation. A key characteristic of PAMAM dendrimers is their pH-accelerated drug release, enabling targeted delivery to pathological sites. [27] Encapsulated drugs exhibit accelerated release in acidic microenvironments, similar to caries-affected areas. [26] Our results showed that EG was successfully loaded and achieved accelerated release under acidic conditions as expected. The carboxylic acid surface groups facilitate peptide conjugation *via* amide bond formation. This improves delivery precision while reducing peptide cytotoxicity. [28] We conjugated AMP G4 to fourth-generation PAMAM-COOH dendrimers *via* amide bond formation between dendrimer carboxylic acids and peptide amine groups. This conjugation strategy yielded a stable nanocomposite that synergistically combines EG, G4 and PAMAM, creating an integrated therapeutic system for comprehensive

View Article Online
DOI: 10.1039/D5TB01477H

caries management.

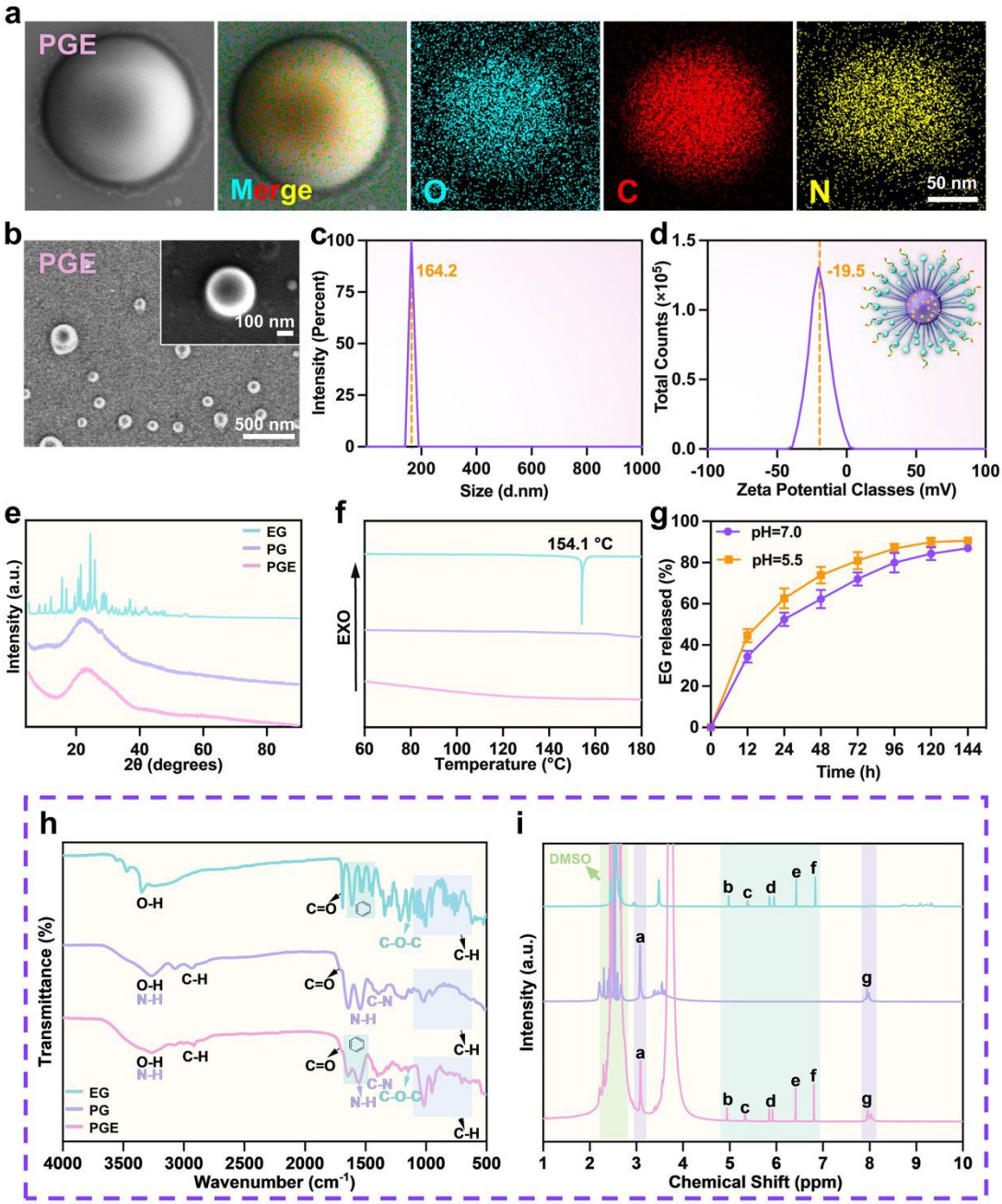

Figure 1. Characterization of PGE NPs. a) EDS elemental mapping displays the spatial distribution of constituent elements (C, O, N) throughout the PGE NPs. **b)** FE-SEM image demonstrating the morphological characteristics of PGE NPs. **c)** DLS analysis showing PGE NPs' size distribution. **d)** Zeta potential measurement indicating surface charge characteristics and colloidal stability of PGE NPs. **e)** XRD patterns comparing crystallinity profiles of EG, PG, and PGE NPs. **f)** DSC thermograms illustrating the thermal behavior of EG, PG, and PGE NPs. **g)** pH-accelerated *in vitro* release profiles of EG from PGE NPs in AS at physiological (pH 7.0) and cariogenic (pH 5.5) conditions. **h)** ATR-FTIR and **i)** ^{h}NMR spectroscopy confirming structural integrity and molecular composition of EG, PG, and PGE NPs.

View Article Online
DOI: 10.1039/D5TB01477H

Cytotoxicity Evaluation:

Given the intimate association between dentin and pulp in the "pulp-dentin complex," and potential contact with oral epithelium, cytotoxicity assessments were performed using HDPCs and HOKs as representative *in vitro* models.

Assessment of PGE Cytocompatibility *via* CLSM and SEM Analysis. Cytoskeletal and nuclear integrity were evaluated using confocal laser scanning microscopy (CLSM) following NPs exposure. Figure 2a demonstrates that treated cells exhibited well-defined nuclei (blue DAPI fluorescence) and extensively developed cytoskeletal architecture with prominent pseudopodia (green FITC-phalloidin-labeled actin). HDPCs and HOKs maintained normal morphology and adhesion patterns following PG and PGE treatment, with cytoskeletal organization comparable to control specimens. Complementary SEM provided high-resolution visualization of three-dimensional cellular morphology (Figure 2b). Cells in control, PG, and PGE groups displayed optimal ultrastructural characteristics, including extensive pseudopodial extension and elaborate intercellular networks facilitating substrate adhesion and cellular spreading. These NPs formulations promoted cytoskeletal organization, enabling complex pseudopodial cross-linking between adjacent cells. Conversely, cells exposed to unencapsulated EG exhibited compromised morphological integrity, characterized by membrane disruption, reduced spreading, and limited pseudopodial development, with visible particle deposition on cellular surfaces suggesting membrane interactions potentially contributing to these alterations. These morphological changes are likely due to the dose-dependent cytotoxicity of EG, wherein higher concentrations induce oxidative stress and apoptosis *via* its pro-oxidant properties. [29]

Evaluation of Cell Proliferation *via* Cell Counting Kit-8 (CCK-8) Assay. Cytotoxicity evaluation revealed that HDPCs and HOKs maintained high viability when exposed to PGE concentrations below 2.5 mg/mL during 24 h incubation (Figure S2). This concentration was therefore established as the optimal working threshold for subsequent experiments. Extended 72 h exposure studies confirmed that both PG and PGE maintained proliferation profiles statistically comparable to controls (Figure 2c). The similar cytocompatibility between PG and control groups demonstrates minimal toxicity following AMP G4 conjugation to PAMAM-

COOH dendrimers. In contrast, cells exposed to unencapsulated EG showed significant proliferation inhibition compared to all other treatment groups.

We selected AMP G4 for optimization based on its superior antimicrobial potency. The high cationic charge density of G4 is essential for its bactericidal efficacy through membrane disruption mechanisms. However, this property promotes nonspecific interactions with mammalian cell membranes, resulting in dose-dependent cytotoxicity that limits clinical application. To overcome this limitation, we employed a charge-modulation strategy by conjugating G4 to PAMAM-COOH dendrimers. This approach leverages electrostatic interactions to neutralize the peptide's excessive cationic charge while preserving its antimicrobial activity. [30-32] Our results validated the effectiveness of this approach. PG demonstrated cytocompatibility comparable to control groups, indicating minimal toxicity to host cells. While EG alone exhibited the highest cytotoxicity profile among all tested formulations, PGE maintained cytocompatibility similar to controls. This protective effect likely results from controlled release kinetics that prevent acute exposure to toxic concentrations and spatial shielding of reactive moieties within the dendrimer architecture. [33]

Collagen Stabilization Assessment:

Quantification of Collagen Protection *via* HYP Analysis. HYP quantification is the gold standard biomarker for collagenolytic activity, where lower concentrations directly indicate enhanced collagen stabilization. [34, 35] To evaluate the collagen-protective effects of our formulations, we conducted quantitative HYP analysis following collagenase challenge in AS (Figures 2d and 2e). Type I collagen was selected as the substrate due to its predominance in oral tissues. Clostridium histolyticum collagenase (Type VII) was an established surrogate for human MMPs in this *in vitro* degradation model, providing standardized and reproducible collagenolytic conditions. The control group exhibited the highest HYP concentration (5.00 ± 0.19 μg/mL), indicating substantial collagen degradation. Treatment with PGE significantly reduced HYP levels to 1.06 ± 0.26 μg/mL, representing a 78.93 ± 4.35% reduction compared to controls. The EG group demonstrated the most effective protection, with HYP levels of 0.47 ± 0.12 μg/mL (90.49 ± 2.56% reduction). The PG group showed intermediate efficacy, achieving 2.46 ± 0.31 μg/mL (50.44 ± 7.81% reduction). These results confirm that both

components contribute to collagen preservation, with their combination in PGE effectively incorporating superior protective properties.

Both EG and PAMAM demonstrate complementary mechanisms for collagen preservation that explain the observed protective effects. EG functions primarily through direct inhibition of MMPs, particularly MMP-9 and MMP-2. [36-38] PAMAM contributes through dual protective mechanisms: first, it chelates essential metal ions such as zinc and calcium that are required for MMP catalytic activity, effectively disrupting enzyme function; second, its amine groups form amide bonds with collagen's carboxylic groups, creating stabilizing cross-links that enhance structural integrity. [39, 40] While the EG group demonstrated superior collagen protection in our assays, its single-component formulation lacked controlled release capabilities, resulting in burst release kinetics and significantly higher cytotoxicity. In contrast, PAMAM encapsulation of EG in the PGE formulation provided controlled drug release that substantially enhanced cytocompatibility while maintaining MMP inhibition efficacy and extending treatment duration, demonstrating the strategic advantage of combining these complementary protective mechanisms within a single delivery system.

View Article Online
DOI: 10.1039/D5TB01477H

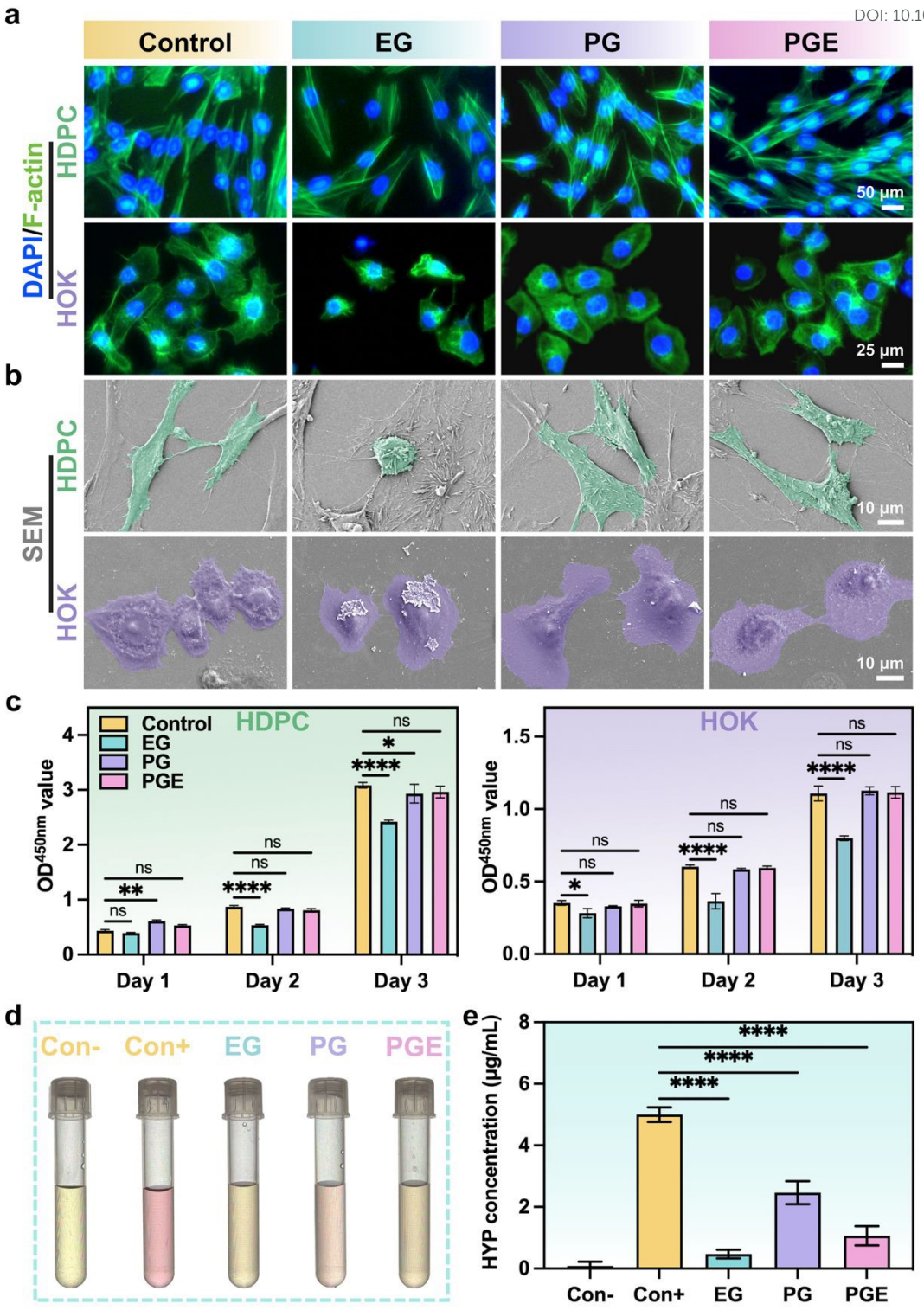

Figure 2. ***In Vitro*** **Biocompatibility and Collagen Stabilization Evaluation. a)** CLSM images showing cellular morphology of HDPCs and HOKs after NPs treatment. Nuclei (blue, DAPI) and F-actin cytoskeleton (green, FITC-phalloidin) demonstrate normal cell spreading. **b)** SEM images revealing ultrastructural details of cellular morphology and pseudopodial extensions. **c)** Cell viability assessment using CCK-8 assay for HDPCs and HOKs following 3-day treatments (n = 3, mean ± SD). **d)** Visual colorimetric changes corresponding to HYP content variations, providing qualitative

assessment of collagen degradation across treatment groups. **e)** HYP quantification results demonstrate the collagen protective efficacy of EG, PG, and PGE formulations compared with negative and positive controls. (Con-represents the negative control without HYP, and Con+ represents the positive control containing 5µg / mL HYP)

Sterilization Assessment:

Determination of PGE Antimicrobial Threshold *via* MIC Analysis. The antimicrobial mechanism of AMP G4 within the PGE formulation operates through direct membrane interaction, causing structural disruption that compromises bacterial cellular integrity. [18] To quantify this antibacterial efficacy, we determined the MIC against *S. mutans*. MIC assessments demonstrated a significant reduction in bacterial viability at PGE concentrations above 2.5 mg/mL, with complete growth inhibition achieved at this threshold (Figure S2). Importantly, this concentration coincides with the previously established cytocompatibility limit, where mammalian cell viability remains uncompromised. Based on this convergence of antimicrobial potency and acceptable cytotoxicity profile, PGE was determined to have an optimal therapeutic window at 2.5 mg/mL, which was subsequently adopted as the standard working concentration for all experimental applications.

Confirmation of PGE's Antimicrobial Activity *via* Spread Plate and TEM Analyses. PGE's bactericidal efficacy against *S. mutans* was evaluated using spread plate methodology and TEM. Figure 3a and Figure 3b demonstrate abundant bacterial colonies in the control group, validating both *S. mutans* viability and absence of contamination. EG and PG treatments exhibited distinct antimicrobial profiles with bacterial survival rates of 53.13 ± 5.64% and 1.20 ± 0.14%, respectively, indicating PG's superior bactericidal properties. PGE demonstrated synergistic antimicrobial activity, reducing bacterial survival to 0.25 ± 0.07%. TEM further revealed the bactericidal mechanism of PGE (Figure 3c). In the control group, bacterial cells exhibited intact cell walls and cytoplasmic membranes with clearly defined boundaries and uniform intracellular density. In contrast, bacteria treated with the PGE showed dramatic morphological changes, including disrupted membranes, cytoplasmic leakage, reduced cellular density, and DNA destruction.

EG's primary therapeutic objective is targeting plaque biofilm. Against planktonic *S. mutans*,

EG employs transcriptional regulation of bacterial stress response pathways, achieving 82-92% downregulation of critical genes, including nox and sodA. [16] These genes encode protective proteins against oxidative damage, and their suppression limits mRNA availability for translation, ultimately impairing essential survival protein synthesis and compromising bacterial viability. However, this approach proves insufficient for planktonic bacteria that lack the protective biofilm matrix, creating a therapeutic gap that necessitates membrane-targeting strategies. AMP G4 addresses this limitation through complementary mechanisms. Upon bacterial contact, G4 adopts a dual-characteristic amphipathic α-helical conformation that enables selective membrane interaction. [18, 20] Positively charged lysine residues electrostatically bind to negatively charged bacterial membrane surfaces, while hydrophobic isoleucine residues penetrate deep into the lipid bilayer core. [41] This coordinated dual interaction compromises membrane integrity, leading to pore formation, cytoplasmic content leakage, and loss of osmotic balance. PAMAM-COOH conjugation strategically preserves G4's bactericidal potency while significantly reducing cytotoxicity concerns. The synergistic combination of G4 and EG in PGE NPs demonstrates enhanced antimicrobial efficacy that substantially exceeds the individual therapeutic contributions of either component alone.

Demonstration of PGE's Efficacy Against Mature *S. mutans* Biofilms *via* SEM and CLSM Analyses. In native caries microenvironments, mature plaque biofilms create dense microbial communities that impede therapeutic agent penetration while sustaining acidogenic activity that drives demineralization. [42] To evaluate biofilm architecture, bacterial morphology, and viability, we developed an *in vitro* model using *S. mutans* biofilms grown with sucrose on human dentin HA substrates. Following treatment with various NPs formulations, we analyzed the samples using SEM and CLSM with Live/Dead fluorescent indicators.

SEM analysis revealed distinct morphological differences between treatment groups (Figure 3d). Control specimens displayed the characteristic ovoid morphology of intact cells. PG-treated specimens exhibited surface irregularities on *S. mutans* with maintained bacterial aggregation, indicating limited biofilm penetration capacity. Both EG and PGE treatment groups demonstrated pronounced structural deterioration, including surface invaginations, volume reduction, and membrane rupture with cytoplasmic extrusion. Live/Dead staining

(Figure 3e) showed predominantly viable bacteria with dense, homogeneous architecture in control specimens. PGE treatment demonstrated the most pronounced bacterial death, with 90.0 ± 2.07% dead bacteria. While EG and PG groups displayed comparable live ratios, EG-treated biofilms exhibited reduced structural integrity, suggesting dead cell detachment due to compromised biofilm cohesion. These observations correlate with SEM findings, validating that EG-encapsulated PGE primarily disintegrates established biofilms while the AMP G4 component compromises bacterial membrane integrity through phospholipid bilayer destabilization.

EG disintegrates established *S. mutans* biofilms through a systematic cascade of complementary mechanisms. The process begins when EG binds to specific amino acid residues GLU 515 and TRP 517 in glucansucrase, inhibiting this essential enzyme responsible for EPS production. [15] This enzymatic disruption immediately reduces glucan synthesis, weakening the biofilm's structural framework. EG simultaneously suppresses critical virulence genes, including gtfB, gtfC, and ftf, which encode proteins necessary for biofilm formation. [16] This genetic downregulation prevents bacteria from producing the components needed to maintain or repair the biofilm structure. As the biofilm disintegrates, EG exploits these vulnerabilities by disrupting cell-to-cell adhesion and intercellular communication networks. This sequential progression—from initial enzymatic inhibition through structural compromise to genetic suppression and metabolic disruption—creates a synergistic cascade that transforms organized, protective bacterial communities into fragmented, vulnerable structures.

Verification of PGE's Effect to Inhibit *S. mutans* Biofilm Formation. In early cariogenesis, *S. mutans* establishes biofilms on the acquired pellicle. [43] The protective EPS shields bacteria from host immune responses and antimicrobial agents, facilitating persistent infection while promoting shifts toward acidogenic populations that accelerate caries progression. [43] Evaluation of NPs formulation efficacy in inhibiting biofilm formation represents a critical research objective. We employed an *in vitro* model using human dentin substrates to co-culture *S. mutans* with various NPs formulations in sucrose-supplemented BHI medium to assess anti-biofilm formation properties.

Biofilm inhibition capacity was quantitatively assessed using CV and SYTO 9 staining (Figure

3f and Figure 3h). Quantitative CV analysis revealed that PGE treatment inhibited biofilm formation by approximately 69.8% relative to control (Figure 3g). SEM of control specimens revealed that *S. mutans* established an interconnected EPS matrix forming a cohesive, dense microbial architecture (Figure 3i). PG-treated specimens demonstrated reduced biofilm density with underlying HA substrate visible in multiple regions. EG and PGE treatment groups exhibited markedly diminished bacterial populations and EPS matrix density, with only isolated short-chain *S. mutans* formations sparsely distributed across the substrate surface. SEM observations corroborated CV and SYTO 9 staining findings. This suggests that PGE can inhibit cariogenic plaque both at the mature stage and at the initial attachment stage. Despite EG demonstrating superior plaque inhibition efficacy (92.9% reduction in CV staining), its notable cytotoxicity, detailed in the previous section, necessitates an optimized delivery approach. Incorporating EG into PG creates a controlled release system that effectively preserves EG's potent biofilm inhibitory properties while minimizing its adverse effects on oral tissues.

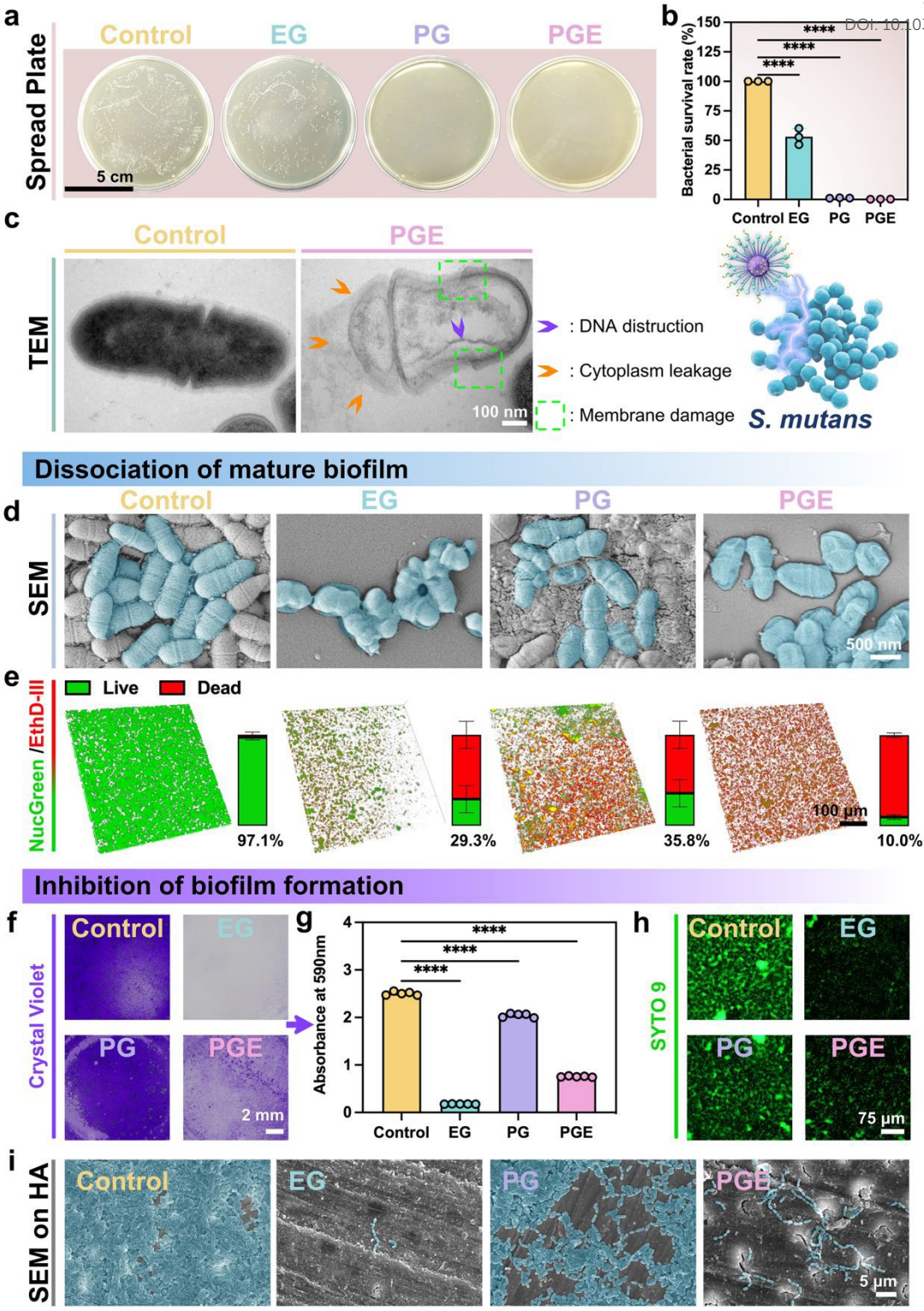

Figure 3. Comprehensive Assessment of Antimicrobial Efficacy on *S. mutans*. a) Representative colony morphology of *S. mutans* following exposure to various NPs formulations. **b)** Quantitative assessment of bactericidal efficacy (mean ± SD, n = 3). **c)** TEM micrographs reveal ultrastructural modifications in bacterial cells exposed to NPs treatments. **d)** SEM images illustrating morphological disintegration of mature *S. mutans* biofilms following NPs treatment. **e)** 3D CLSM images and quantitative analysis depicting Live/Dead

View Article Online
DOI: 10.1039/D5TB01477H

fluorescence staining of mature *S. mutans* biofilms following NPs exposure, presented as percentage of live versus dead bacterial cells. **f)** Evaluation of biofilm inhibition capacity using CV staining. **g)** Quantitative analysis of CV staining (mean ± SD, n = 6). **h)** Complementary biofilm staining by SYTO 9 fluorescence. **i)** SEM images illustrating the inhibition of *S. mutans* biofilm formation capacities on HA slices following NPs treatment.

Remineralization of Demineralized Dentin *In Vitro* without or with Collagenase:

Dentin remineralization requires two essential components: type I collagen as the mineralization template and a mechanism to drive mineral deposition. [44] *In vitro* studies confirm that PGE complexes retain PAMAM's mineralization capacity while preserving EG's MMPs inhibition, demonstrating synergistic efficacy in dentin restoration.

Assessment of Dentin Remineralization *via* SEM Analysis. EDTA-treated specimens exhibited exposed collagen matrices with minimal crystalline structures, confirming effective demineralization (Figure 4a). This model simulated clinical conditions where bacterial acids dissolve mineral phases, leaving vulnerable collagen fibrils. The DDW control group showed patent tubules, progressive collagen degradation, and pronounced interfibrillar spacing, demonstrating limited spontaneous repair capacity. The EG group maintained dense collagen matrices despite empty tubules, indicating practical collagen preservation without mineral deposition. PAMAM-based formulations (PG and PGE) demonstrated enhanced remineralization outcomes. The PG group exhibited inconsistent mineralization with regional variability. In contrast, PGE achieved comprehensive intratubular mineral recovery with superior uniformity.

Verification of Dentin Topography Restoration *via* Confocal Morphometric Analysis. White light confocal analysis characterized dentin surface topography (Figure 4b). EDTA demineralization transformed the homogeneous structure of intact dentin into irregular surfaces with significantly reduced, heterogeneously distributed dentinal tubules. PGE treatment resulted in substantial surface restoration, characterized by extensive tubular occlusion and enhanced surface uniformity.

Evaluation of Dentin Hardness Recovery Under Collagenase Challenge *via* Vickers Hardness Analysis. Microhardness testing evaluated mechanical property recovery (Figures 4c and S5). The DDW and EG group showed negligible hardness recoveries regardless of collagenase presence. Without collagenase, PG and PGE groups demonstrated comparable hardness recovery. However, with

collagenase challenge, PGE exhibited significantly superior hardness recovery compared to PG, restoring EDTA-demineralized dentin to 89.88 ± 4.5% of intact values.

Confirmation of Collagen Preservation and Mineral Deposition *via* ATR-FTIR Spectroscopy Analysis. ATR-FTIR analysis (Figure 4d) evaluated dentin remineralization by examining two key spectral bands. The amide I band (1655 cm^{-1}) represents C=O stretching in collagen, while the PO_4^{3-} band (950–1150 cm^{-1}) indicates phosphate groups in HA. These bands correspond to collagen's peptide and HA's P-O bonds. The amide I band (1655 cm^{-1}) showed significantly enhanced intensity in EG, PG, and PGE groups compared to DDW controls. The PO_4^{3-} absorption band (950-1150 cm^{-1}) demonstrated a clear hierarchical intensity pattern: PGE > PG > EG > DDW. This graduated profile directly correlates with mineral content and confirms the superior remineralization efficacy of PGE.

HYP Analysis in Collagenase-Treated Model. HYP concentration assessment revealed differential collagen preservation (Figure 5e). The PGE group demonstrated significantly lower HYP levels than PG, indicating superior dentinal collagen matrix integrity preservation under collagenase challenge.

Confirmation of the dentin components *via* EDS Analysis. The calcium-to-phosphorus (Ca/P) ratio serves as a critical indicator of dentin remineralization quality, reflecting mineral composition (Figure 5f). According to its chemical formula $Ca_{10}(PO_4)_6(OH)_2$, healthy dentin HA exhibits a theoretical stoichiometric value of 1.67. [45] EDTA-induced demineralization significantly increased the Ca/P ratio to 1.9988 ± 0.1319, indicating preferential phosphate loss during demineralization. This elevation occurs because phosphate exhibits greater solubility under acidic or chelating conditions than Ca^{2+}. [46] Among treatment groups, DDW (1.9352 ± 0.0357) and EG (1.9503 ± 0.1402) showed limited variation in Ca/P ratios compared to the demineralized group. In contrast, PG treatment reduced the ratio to 1.7055 ± 0.1123, indicating enhanced mineral recovery. Most notably, the PGE composite achieved the lowest Ca/P ratio at 1.6493 ± 0.0339, which closely approximated intact dentin values and demonstrated near-ideal restoration of the mineral structure.

Confirmation of HA Formation *via* XRD Analysis. XRD analysis characterized mineral phase composition (Figure 4g). PGE and PG-treated specimens demonstrated prominent HA-characteristic diffraction peaks at (002), (211), (300), and (310) crystallographic planes. These patterns indicated

newly formed mineral phases consisted predominantly of HA with crystallographic properties analogous to intact dentin.

Demineralized dentin exhibits inherent limitations for spontaneous repair. Progressive collagen degradation occurs under uncontrolled MMPs activity and without remineralization nucleation templates. EG demonstrates practical collagen preservation through dual mechanisms: zinc chelation at MMPs' active sites and formation of stabilizing non-covalent interactions with collagen fibrils. [13, 14] This mitigates degradation of collagen fibers that would otherwise undermine the structural foundation essential for effective remineralization. However, EG's function remains primarily protective rather than actively promoting mineral formation. Therefore, PAMAM-COOH is required to facilitate dentin remineralization. Initially, the dendrimer establishes strong binding to demineralized dentin *via* electrostatic interactions between carboxyl groups and positively charged collagen residues (lysine, arginine). The dendrimer's molecular weight enables retention within collagen fibrils through both electrostatic and size-exclusion mechanisms. It also enhances collagen stability through covalent amide bond formation. [39, 40] Subsequently, the highly branched PAMAM architecture provides multiple binding sites for mineral precursors. Terminal carboxyl groups promote Ca^{2+} chelation, forming stable intermediates that attract PO_4^{3-} ions. This process concentrates mineral precursors at specific nucleation sites, enabling controlled mineral formation. Finally, the dendrimer framework stabilizes amorphous calcium phosphate (ACP) precursors, transforming them into organized HA crystals. [47] The superior performance of the PGE combination demonstrates synergistic remineralization mechanisms. EG provides immediate and sustained collagen protection, preventing matrix degradation during remineralization. PAMAM-COOH simultaneously establishes nucleation sites and facilitates controlled mineral deposition. The combination ensures that both organic scaffold integrity and mineral nucleation proceed optimally. This results in a comprehensive restoration closely approximating natural dentin composition and structure.

View Article Online
DOI: 10.1039/D5TB01477H

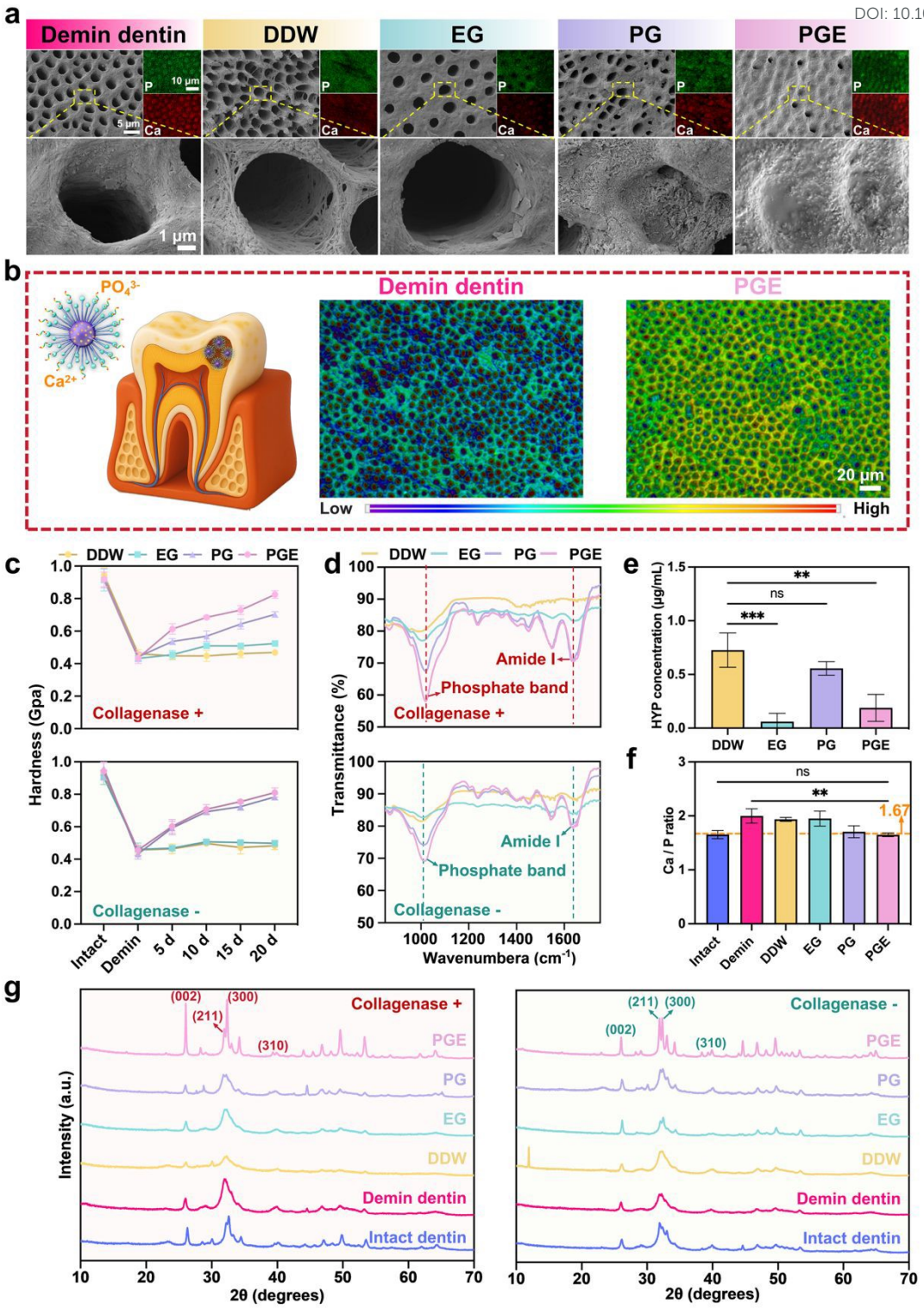

Figure 4. ***In Vitro*** **Dentin Remineralization. a)** SEM images and EDS elemental mapping of calcium and phosphorus distribution following 20-day remineralization in AS with collagenase. **b)** 3D confocal surface profilometry revealing topographical modifications of dentin surfaces following remineralization treatments. **c)** Temporal progression of Vickers hardness values for intact dentin, EDTA-demineralized dentin, and remineralized specimens (days 5, 10, 15, 20) in models with and without collagenase. **d)** ATR-FTIR spectra in models with and without collagenase show characteristic

View Article Online
DOI: 10.1039/D5TB01477H

phosphate and Amide I peaks, indicating mineral and organic matrix changes. **e)** HYP concentration in AS solution from the collagenase degradation model (mean ± SD, n = 3). **f)** Ca/P ratios of dentin after treatments. Relative calcium and phosphorus content percentages in each treatment group (mean ± SD, n = 3). **g)** XRD patterns comparing intact dentin, EDTA-demineralized dentin, and remineralized specimens in models with and without collagenase. Characteristic HA peaks (002), (211), (300), and (310) demonstrate mineral phase restoration.

In Vivo Antimicrobial and Anti-caries Efficacy of PGE NPs:

Figure 6a illustrates surgical protocols for investigating PGE NPs' efficacy in SD rats. Body weight measurements remained consistent across all experimental groups throughout the study period (Figure S3), with no observable oral mucosal pathologies or organ abnormalities. Histological evaluation using H&E staining (Figure 6h and S4) confirmed biocompatibility, revealing no significant inflammatory infiltrate or pathological alterations.

Saliva *S. mutans* Detection *via* CFUs Analysis. Upon completion of the *in vivo* experiment, saliva specimens from each group were cultured on mitis salivarius bacitracin (MSB) selective agar (Figure 6b). [48] Microbiological analysis demonstrated abundant CFUs in control specimens. Quantitative assessment of CFUs revealed a gradient of antimicrobial efficacy: PG > EG > PGE. The survival rate of *S. mutans* in PGE-treated specimens was notably reduced to 0.6926 ± 0.4154% (Figure 6c).

Assessment of Caries Lesions *via* Microscopic and Radiographic Analysis. After caries intervention, sagittal and transverse sections of rat mandibular specimens were visualized under stereomicroscopy (Figure 6d). Control specimens exhibited moderate to extensive pit and fissure lesions, whereas PGE-treated specimens showed minimal carious involvement. PG and EG groups displayed no macroscopic structural defects but exhibited discernible subsurface translucent demineralization zones. The Keyes scoring system evaluated lesions based on progression depth: enamel-limited (E), superficial dentinal (Ds), moderate dentinal (Dm), and extensive dentinal (Dx). Comprehensive scores (Figure 6e) demonstrated significantly reduced values across all lesion categories in PGE-treated specimens compared to controls. Both PG and EG groups exhibited lower scores than controls, with PG demonstrating superior caries-inhibitory effects.

Micro-CT images of molar regions (Figure 6g) showed profound pit and fissure radiolucencies with partial structural loss in control specimens, linear subsurface dentin radiolucencies in EG-treated specimens, and milder focal radiolucencies in PG-treated specimens, while PGE-treated specimens

showed minimal evidence of dentin lesions. Quantitative mineral density analysis within 200 μm sub-enamel dentin (Figure 6f) demonstrated: PGE (1081.5296 ± 46.096 mg/mL) > PG (969.6377 ± 18.466 mg/mL) > EG (809.0689 ± 17.066 mg/mL) > Control (744.5263 ± 16.721 mg/mL).

While *in vitro* studies elucidate fundamental interactions and mechanisms, they cannot replicate the oral environment's complexity, including salivary composition, pH fluctuations, enzymatic activity, and dynamic tissue responses. Our *in vivo* experiments were essential to evaluate PGE NPs under near-clinical conditions. The results demonstrate that PGE intervention inhibits both *S. mutans* colonization and dentin caries progression under physiological conditions. The superior performance of PGE compared to individual components (PG and EG) suggests synergistic antimicrobial and remineralization effects that warrant further investigation for translational applications. The absence of inflammatory responses or pathological alterations in treated specimens further supports the biocompatibility profile of these NPs. In conclusion, Keyes scoring and micro-CT analysis confirm that PGE intervention inhibits dentin caries initiation and progression *in vivo*.

View Article Online
DOI: 10.1039/D5TB01477H

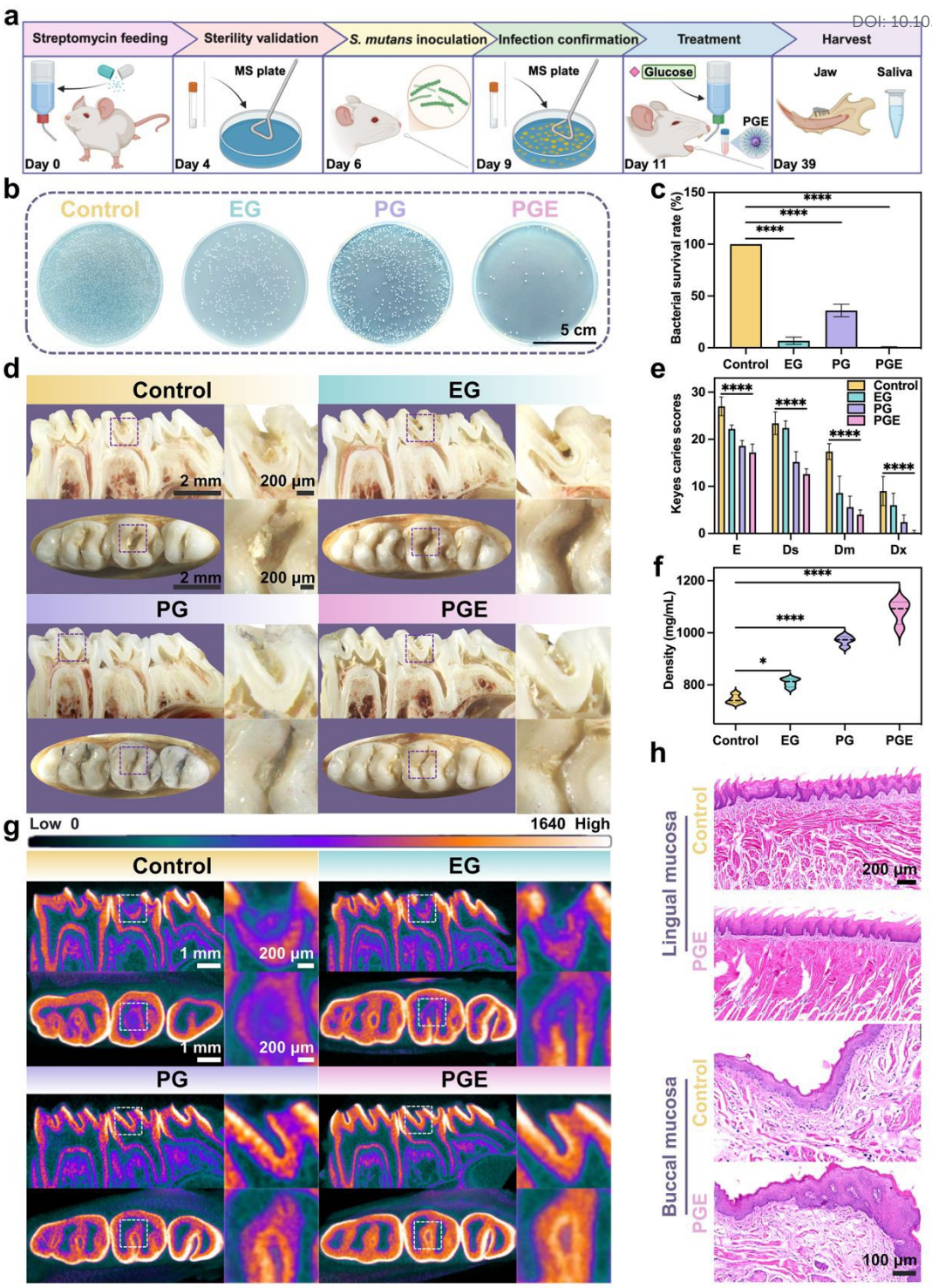

Figure 5. ***In Vivo*** **Therapeutic Efficacy Against Dentin Caries. a)** Schematic diagram of the animal experiment design and treatment protocol timeline. **b)** MSB agar plates showing bacterial growth following 39-day treatment. **c)** Quantitative bactericidal efficacy *in vivo* (mean ± SD, n = 3). **d)** Representative images for Keyes scoring assessment of caries severity. **e)** Caries score results using Keyes method (E = enamel caries, Ds = slight dentinal, Dm = moderate dentinal, Dx = extensive dentinal, Oc = occlusal, Ss = smooth surface). **f)** Mineral density analysis of dentin within 200 μm beneath enamel, quantifying remineralization efficacy (mean ± SD, n = 3). **g)** Micro-CT images of molar regions showing carious lesion extent across treatment groups. **h)** Histological sections of

lingual (upper) and buccal (lower) mucosa for control and PGE groups, showing no inflammatory response or tissue pathology.

Conclusions

In this study, we developed PGE, an innovative nanoplatform that integrates biofilm-disintegrative, antibacterial, collagen-stabilizing, and remineralizing properties to provide a comprehensive approach for dentin caries treatment. Our extensive *in vitro* and *in vivo* evaluations demonstrate PGE's ability to counteract caries' etiological factors, including bacterial proliferation, biofilm formation, collagen degradation, and mineral loss. The strategic combination of AMP G4 with the bioactive polyphenol EG, encapsulated within the PAMAM-COOH dendrimer framework, generates synergistic effects that effectively address the multifaceted pathogenesis of dentin caries. This research highlights the transformative potential of nanotherapeutic approaches in dental science and establishes a foundation for developing next-generation biomaterials designed to optimize oral health.

Author Contributions

Mingxiao Liu: Conceptualization, Data Curation, Formal Analysis, Validation, Writing - Original Draft, Writing - Review & Editing. Jiahe Li, Ziyou Wang: Data Curation, Validation, Writing - Original Draft. Miao Chen: Funding Acquisition, Validation, Resources, Supervision, Methodology. Jianru Yi, Kunneng Liang, Zhihe Zhao: Conceptualization, Funding Acquisition, Project Administration, Supervision, Writing - Review & Editing.

Conflicts of Interest

There are no conflicts to declare.

Data Availability

Data will be made available on request.

Acknowledgements

This research was supported by the National Natural Science Foundation of China (grant numbers 82270970, 82470967, 32271416), International Orthodontics Foundation Young

Grants Award (grant number IOF2022Y04), and Natural Science Foundation of Sichuan Province (grant numbers 2025ZNSFSC1591, 2025ZNSFSC1587). We acknowledge and appreciate BioRender for providing the feature icons utilized in Figure 6a, which significantly enhanced the visual communication of our methodology.

References

1. N. J. Kassebaum, A. G. C. Smith, E. Bernabé, T. D. Fleming, A. E. Reynolds, T. Vos, C. J. L. Murray and W. Marcenes, *J. Dent. Res.*, 2017, **96**, 380–387.
2. X. Cai, B. Han, Y. Liu, F. Tian, F. Liang and X. Wang, *ACS Appl. Mater. Interfaces*, 2017, **9**, 12949–12958.
3. E. A. Münchow, A. F. da Silva, E. Piva, C. E. Cuevas-Suárez, M. T. P. de Albuquerque, R. Pinal, R. L. Gregory, L. Breschi and M. C. Bottino, *J. Mater. Chem. B*, 2020, **8**, 5477–5487.
4. J. Yang, J. Huang, H. Qin, J. Long, X. Lin and F. Xie, *J. Biomater. Sci. Polym. Ed.*, 2022, **33**, 668–686.
5. N. B. Pitts, D. T. Zero, P. D. Marsh, K. Ekstrand, J. A. Weintraub, F. Ramos-Gomez, J. Tagami, S. Twetman, G. Tsakos and A. Ismail, *Nat. Rev. Dis. Primers*, 2017, **3**, 17030.
6. Y. Zhang, Y. Liu, F. Fan, H. Zhang, Q. Xin, S. Sun, X. Xu, L. Zheng, Y. Liu, C. Ding, M. Ding and J. Li, *J. Mater. Chem. B*, 2025, **13**, 4214–4224.
7. S. Liu, R. Chen, Y. Wang, W. Zhang, Z. Zhang, Y. Hou, L. He, F. Tian and S. Liu, *Mater. Chem. Front.*, 2024, **8**, 836–850.
8. X. Wang, Q. Chen, J. Li, W. Tian, Z. Liu and T. Chen, *J. Mater. Chem. B*, 2024, **12**, 7497–7518.
9. J. M. ten Cate and M. A. R. Buzalaf, *J. Dent. Res.*, 2019, **98**, 725–730.
10. M. Kashi, M. Varseh, Y. Hariri, Z. Chegini and A. Shariati, *Front. Pharmacol.*, 2025, **16**, 1548117.
11. F. Gao, B. Li, W. Zhang, H. Wang, Y. Dai, X. Li, W. Zhang, X. Zhang, J. Mao, S. Zhao, S. Zhang, A. Zargul, Y. Zhang, J. Tang and J. Liu, *Nano Lett.*, 2025, **25**, 5181–5192.
12. G. Pan, J. Zheng, Z. Li, Q. Duan, M. Zhang and D. Wang, *J. Mater. Chem. B*, 2025, **13**, 3730–3743.
13. A. Prakki, Y. Xiong, J. Bortolatto, L. L. Gonçalves, A. Bafail, G. Anderson and A. T. Stavroullakis, *Dent. Mater.*, 2018, **34**, 1625–1633.
14. S. Liao, Y. Tang, C. Chu, W. Lu, B. Baligen, Y. Man and Y. Qu, *J. Biomed. Mater. Res. A*, 2020, **108**, 2395–2408.
15. M. G. B. Aragão, X. He, C. P. Aires and S. A. M. Corona, *Arch. Oral Biol.*, 2024, **164**, 105990.
16. C. Kong, H. Zhang, L. Li and Z. Liu, *J. Oral Microbiol.*, 2022, **14**, 2131117.
17. R. Spohn, L. Daruka, V. Lázár, A. Martins, F. Vidovics, G. Grézal, O. Méhi, B. Kintses, M. Számel, P. K. Jangir, B. Csörgő, Á. Györkei, Z. Bódi, A. Faragó, L. Bodai, I. Földesi, D. Kata, G. Maróti, B. Pap, R. Wirth, B. Papp and C. Pál, *Nat. Commun.*, 2019, **10**, 4538.
18. M. Liao, H. Gong, X. Quan, Z. Wang, X. Hu, Z. Chen, Z. Li, H. Liu, L. Zhang, A. J. McBain, T. A. Waigh, J. Zhou and J. R. Lu, *Small*, 2023, **19**, 2204428.
19. J. Zhang, C. Chen, J. Chen, S. Zhou, Y. Zhao, M. Xu and H. Xu, *ACS Appl. Mater. Interfaces*,

View Article Online
DOI: 10.1039/D5TB01477H

2020, **12**, 27866–27875.
20. H. Wang, M. Niu, T. Xue, L. Ma, X. Gu, G. Wei, F. Li and C. Wang, *J. Mater. Chem. B*, 2022, **10**, 1858–1874.
21. J. Li, M. Fan, Z. Jiao, Y. K. Chan, L. Cheng, J. Li, Y. Deng and K. Liang, *Nano Today*, 2024, **59**, 102541.
22. S. Tao, J. Yang, Z. Su, F. Zhou, Z. Wang, Y. Yang, L. Sun, Y. Deng, K. Liang and J. Li, *Small*, 2022, **18**, e2203644.
23. B. Horev, M. I. Klein, G. Hwang, Y. Li, D. Kim, H. Koo and D. S. Benoit, *ACS Nano*, 2015, **9**, 2390–2404.
24. H. Kheraldine, O. Rachid, A. M. Habib, A. E. Al Moustafa, I. F. Benter and S. Akhtar, *Adv. Drug Deliv. Rev.*, 2021, **178**, 113908.
25. S. Tao, X. Yang, L. Liao, J. Yang, K. Liang, S. Zeng, J. Zhou, M. Zhang and J. Li, *Dent. Mater.* , 2021, **37**, 1337–1349.
26. F. Abedi-Gaballu, G. Dehghan, M. Ghaffari, R. Yekta, S. Abbaspour-Ravasjani, B. Baradaran, J. E. N. Dolatabadi and M. R. Hamblin, *Appl. Mater. Today*, 2018, **12**, 177–190.
27. M. Zhang, J. Zhu, Y. Zheng, R. Guo, S. Wang, S. Mignani, A. M. Caminade, J. P. Majoral and X. Shi, *Pharmaceutics*, 2018, **10**, 162.
28. Z. Cui, Q. Luo, M. S. Bannon, V. P. Gray, T. G. Bloom, M. F. Clore, M. A. Hughes, M. A. Crawford and R. A. Letteri, *Biomater. Sci.*, 2021, **9**, 5069–5091.
29. S. Liu, Z. Sun, P. Chu, H. Li, A. Ahsan, Z. Zhou, Z. Zhang, B. Sun, J. Wu, Y. Xi, G. Han, Y. Lin, J. Peng and Z. Tang, *Apoptosis*, 2017, **22**, 672–680.
30. A. W. Young, Z. Liu, C. Zhou, F. Totsingan, N. Jiwrajka, Z. Shi and N. R. Kallenbach, *Med. Chem. Commun.*, 2011, **2**, 308–314.
31. A. Narsireddy, K. Vijayashree, M. G. Adimoolam, S. V. Manorama and N. M. Rao, *Int. J. Nanomed.*, 2015, **10**, 6865–6878.
32. S. Sadekar and H. Ghandehari, *Adv. Drug Deliv. Rev.*, 2012, **64**, 571–588.
33. V. M. Thanh, T. H. Nguyen, T. V. Tran, U. P. Ngoc, M. N. Ho, T. T. Nguyen, Y. N. T. Chau, V. T. Le, N. Q. Tran, C. K. Nguyen and D. H. Nguyen, *Mater. Sci. Eng. C Mater. Biol. Appl.*, 2018, **82**, 291–298.
34. M. S. Islam, S. J. Khunkar, S. Nakashima, A. Sadr, T. Nikaido and J. Tagami, *J. Dent.*, 2016, **47**, 94–97.
35. R. Wang, S. Nisar, Z. Vogel, H. Liu and Y. Wang, *Dent. Mater.*, 2022, **38**, 748–758.
36. C. Chu, J. Deng, Y. Man and Y. Qu, *Biomed. Res. Int.*, 2017, **2017**, 5615647.
37. Y. Liu, H. Yang, K. Qiu, K. Li, J. Yu, C. Yao and C. Huang, *J. Dent.* , 2025, **160**, 105895.
38. S. Alhijji, J. A. Platt, A. Alhotan, N. Labban, M. C. Bottino and L. J. Windsor, *Nanomaterials*, 2023, **13**, 999.
39. J. Fan, P. Wang, S. Wang, R. Li, Y. Yang, L. Jin, Y. Sun and D. Li, *Discov. Nano*, 2025, **20**, 40.
40. V. Beghetto, V. Gatto, S. Conca, N. Bardella and A. Scrivanti, *Molecules*, 2019, **24**, 3361.
41. J. Zhang, H. Gong, M. Liao, Z. Li, R. Schweins, J. Penny and J. R. Lu, *J. Colloid Interface Sci.*, 2022, **608**, 193–206.
42. T. Phuangkaew, N. Booranabunyat, S. Kiatkamjornwong, P. Thanyasrisung and V. P. Hoven, *Carbohydr. Polym.*, 2022, **277**, 118882.
43. Y. Lin, J. Chen, X. Zhou and Y. Li, *Crit. Rev. Microbiol.*, 2021, **47**, 667–677.

44. L. Zhang, Z. Zhou, Z. Liu, Y. Shi, Y. Mao, B. Fu and Z. Wang, *Int. J. Biol. Macromol.*, 2025, **308**, 142402.
45. A. Diez-Escudero, M. Espanol and M. P. Ginebra, *Chem. Sci.*, 2023, **15**, 55–76.
46. F. R. Tay and D. H. Pashley, *Biomaterials*, 2008, **29**, 1127–1137.
47. K. Liang, S. Wang, S. Tao, S. Xiao, H. Zhou, P. Wang, L. Cheng, X. Zhou, M. D. Weir, T. W. Oates, J. Li and H. H. K. Xu, *Int. J. Oral Sci.*, 2019, **11**, 15.
48. J. Li, L. Zhou, M. Liu, X. He and T. Huang, *Tissue Eng. Part C Methods*, 2025, **31**, 230–236.

View Article Online
DOI: 10.1039/D5TB01477H

Data Availability Statement

The data that support the findings of this study are available in the supplementary material of this article.